drones

MDPI

Article

An Approach to Air-to-Surface Mission Planner on 3D Environments for an Unmanned Combat Aerial Vehicle

Ji-Won Woo, Yoo-Seung Choi, Jun-Young An and Chang-Joo Kim *

Department of Aerospace and Information Engineering, Konkuk University, Seoul 05029, Korea; wjw1542@konkuk.ac.kr (J.-W.W.); chldbtmd1234@konkuk.ac.kr (Y.-S.C.); denix717@konkuk.ac.kr (J.-Y.A.)
* Correspondence: cjkim@konkuk.ac.kr

Abstract: Recently, interest in mission autonomy related to Unmanned Combat Aerial Vehicles(UCAVs) for performing highly dangerous Air-to-Surface Missions(ASMs) has been increasing. Regarding autonomous mission planners, studies currently being conducted in this field have been mainly focused on creating a path from a macroscopic 2D environment to a dense target area or proposing a route for intercepting a target. For further improvement, this paper treats a mission planning algorithm on an ASM which can plan the path to the target dense area in consideration of threats spread in a 3D terrain environment while planning the shortest path to intercept multiple targets. To do so, ASMs are considered three sequential mission elements: ingress, intercept, and egress. The ingress and egress elements require a terrain flight path to penetrate deep into the enemy territory. Thus, the proposed terrain flight path planner generates a nap-of-the-earth path to avoid detection by enemy radar while avoiding enemy air defense threats. In the intercept element, the shortest intercept path planner based on the Dubins path concept combined with nonlinear programming is developed to minimize exposure time for survivability. Finally, the integrated ASM planner is applied to several mission scenarios and validated by simulations using a rotorcraft model.

Keywords: air-to-surface mission; mission autonomy; path planning; unmanned combat aerial vehicle; trajectory tracking

check for updates

Citation: Woo, J.-W.; Choi, Y.-S.; An, J.-Y.; Kim, C.-J. An Approach to Air-to-Surface Mission Planner on 3D Environments for an Unmanned Combat Aerial Vehicle. *Drones* **2022**, *6*, 20. https://doi.org/10.3390/drones6010020

Academic Editor: Higinio González Jorge

Received: 23 December 2021
Accepted: 10 January 2022
Published: 12 January 2022

Publisher's Note: MDPI stays neutral with regard to jurisdictional claims in published maps and institutional affiliations.

Copyright: © 2022 by the authors. Licensee MDPI, Basel, Switzerland. This article is an open access article distributed under the terms and conditions of the Creative Commons Attribution (CC BY) license (https://creativecommons.org/licenses/by/4.0/).

1. Introduction

Air-to-surface missions (ASMs) are becoming increasingly dangerous in modern warfare, where the successful performance of ASMs is strategically important. To deal with this issue, missions are carried out using stealth aircraft to avoid threats on recent battlefields. However, developing an aircraft with stealth capabilities is costly and does not exclude threats to pilots' lives altogether. Performing ASMs using Unmanned Combat Aerial Vehicles (UCAVs) is an effective approach to handling these difficulties. For this reason, many studies have been conducted to perform missions using UCAVs. Through these efforts, several approaches are proposed to efficiently plan ASMs [1–14] in Table 1. Randal W Beard et al. [1] proposed an ASM planning algorithm for multiple UCAVs. The proposed algorithm plans the path based on the Voronoi-diagram concept and assigns the targets to UCAVs to minimize the prescribed objective function. Path planning based on the Voronoi diagram concept is advantageous for planning a path, which bypasses threats to the maximum extent. However, with the cost of creating unnecessary detours. Yeonju Eun et al. [2] proposed a path planner which combines the Voronoi-diagram concept and potential field concept to address this issue for Suppression to Enemy Air Defenses(SEAD) mission planning. There is a limitation that these algorithms are only applied to two-dimensional environments. H.H Triharminto et al. [3], proposed a path planner for moving target intercept on dynamic 3D environments, but the algorithm focuses only on local environments. Meanwhile, several path planners using Dubins path concept for target intercept were proposed [4–6]. These approaches have the advantage of being able to

consider the dynamic constraints of aircraft and simply generate an optimal path. However, it has not been verified in a three-dimensional environment. Most of the proposed studies focus on generating paths to approach targets in a 2D global environment or generate only a path to pursue and intercept a target in a 3D environment. To contribute to this issue, an ASM planning technique that can simultaneously plan the path to approach the targets and the path to hit the targets while considering both threats and obstacles in the 3D environment is addressed in this paper.

Table 1. ASM Planner's characteristics of the literature [1–14].

	Planning on 2D Environment	**Planning on 3D Environment**
Planning in Global Map to Approaching the Targets/Target Clustered Area	[1,2,4,7,8,11,14]	[13]
Planning in Local Map to Pursuing/Intercepting the Targets	[5,6,9,12]	[3,10]

ASMs are classified into several detailed missions, depending on the mission's environment and goals as follows: Air Interdiction (AI), Close Air Support (CAS), Suppression to Enemy Air Defenses (SEAD), and Attack Operations (AO). According to the U.S. Air Force Doctrine [15,16], AO and SEAD missions fall under the category of Offensive Counterair(OCA) missions, while AI and CAS missions belong to the category of counterland missions. AO is intended to destroy, disrupt, or degrade counterair targets including enemy air and missile threats, their command and control, and their support infrastructure on the ground such as airfields, launch sites, launchers, fuel, supplies, etc. The SEAD missions aim to neutralize, destroy, or degrade enemy surface-based air defenses by destructive or disruptive means. While AO focuses on preventive measures to strike the enemy air defense assets before they are deployed, there is a difference that the SEAD mission aims to neutralize the already deployed enemy air defense assets. On the other hand, the AI missions' goal is to preemptively disrupt, delay, or destroy the enemy's military potential before it responds effectively to friendly forces. Whereas the CAS mission aims to strike against hostile targets that are near close to friendly forces. Since the enemy targets are near friendly forces, tracking of friendly forces' movements and careful firing on targets are more crucial than in the case of the AI missions. However, since the targets of AI missions are usually within enemy territory, the number of interspersed threats within the mission environment is likely to be greater than that of CAS missions.

These ASMs have in common that they basically perform consecutive mission elements of ingress, intercept, and egress. The ingress mission element is the phase of approaching the intercept mission area while avoiding the various threats that appear when entering a hostile area. Then, the aircraft intercepts the target quickly and accurately in the intercept mission element. Lastly, the egress mission element is the phase of escaping the hostile area while avoiding scattered threats. Since the ASM planner can be designed through a strategy of sequential planning on each mission element. For ingress and egress missions, avoiding enemy radar detection and air defense threats are foremost important. Stealth aircraft may be a solution, but detection avoidance through low-fly flight maneuvers which is called hedgehop can also be a good approach. Therefore, a terrain flight path planner is proposed to generate a contour chasing flight path for the ingress and egress mission element maneuver path planning. In the intercept phase, it is important to strike the target as quickly as possible rather than avoiding the threats. Thus, an algorithm is proposed that can generate the shortest target intercept path in this paper.

The paper is structured as follows. In Section 2, terrain and threat modeling techniques are treated to describe the real-world battlefield environments. Terrain flight path planner based on RRT* algorithm that can generate asymptotic global optimal path is addressed in Section 3. The shortest target intercept path planner is addressed in Section 4. In Section 5, several test scenarios are presented for the validation of the presented mission planner. In

Section 6, The integrated mission planner is validated through applications on the proposed scenarios. Furthermore, simulations are performed using a rotorcraft model to track the generated trajectories. Section 7 provides the important details and analysis of the results are summarized in the conclusion.

2. Mission Environment Construction

Building a virtual mission environment is crucial when designing path planning algorithms for ASMs. Therefore, this section treats the techniques used to increase the applicability of the designed path planner when building the real battlefield environment including terrain threat models. The terrain height model of the real world is inserted into the planning environment to describe actual battlefields such as in Figure 1. The maximum height of the terrain is 591 m while both the X-axis and Y-axis are 13,745.58 m wide. The terrain map was generated based on the terrain heightmap near 37°25′20.2″ N, 127°01′21.9″ E.

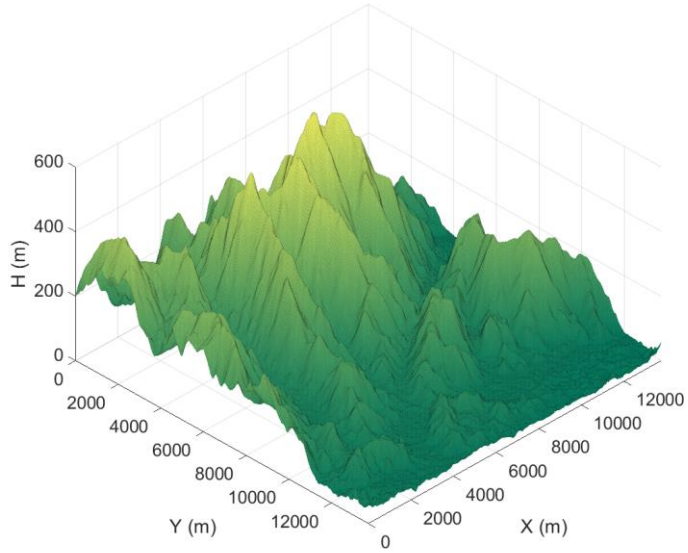

Figure 1. Terrain model.

In addition, a spherical threat model is proposed which has a radius of maximum threat reach and Radial Basis Function (RBF) based threat strength distribution in the inner domain of the sphere to describe common threat types. Equation (1) shows the threat strength distribution in the inner domain of the threat:

$$f_{threat}(R, R_{\max}, s_{threat}, \varepsilon_r) = \begin{cases} s_{threat} \cdot \varphi(R, \varepsilon_r), & (R \leq R_{\max}) \\ 0.0, & (R > R_{\max}) \end{cases} \quad \text{where, } R = \|\boldsymbol{r} - \boldsymbol{r}_{threat}\|_2 \tag{1}$$

$$\varphi_{Gaussian}(R, R_{\max}, \varepsilon_r) = e^{-0.5 \cdot (R/R_{\max})^2/\varepsilon_r} \tag{2}$$

where $\boldsymbol{r}$ represents the position vector of a node, and $\boldsymbol{r}_{threat}$ represents the position vector of a threat. The strength of the threat center is s_{threat}, and the proportion of the threat varies according to the distance from the center of the threat and the RBF shape factor ε_r. Furthermore, the threat disappears when it is outside of the maximum threat distance. In this paper, the Gaussian function shown in Equation (2) is selected as the threat distribution [17]. Other types of RBF can also be adopted depending on the mission environment. Figure 2 represents an example of a terrain map with five threat models.

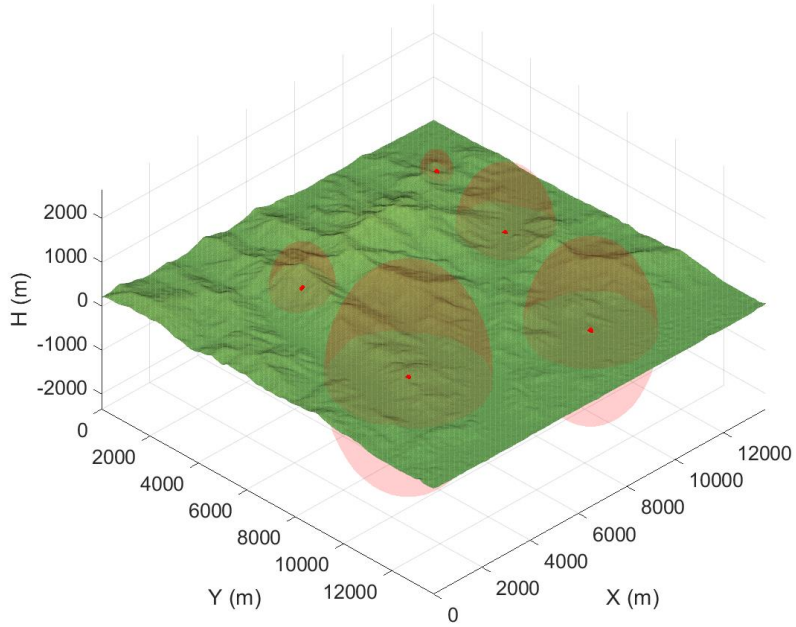

Figure 2. An example of terrain map with five threat models.

3. Terrain Flight Path Planner

UCAVs must avoid multiple threats in the hostile area to perform ingress and egress mission elements. Therefore, there is a need for a Terrain Flightpath planner which is capable of avoiding threats while avoiding detection of enemy radar through a low approach. There are a number of path planning algorithms that can be applied to this problem. Path Planning algorithms are commonly classified into five different categories [18]: sampling-based algorithms, node-based algorithms, mathematic model-based algorithms, bio-inspired algorithms, and multifusion-based algorithms. Among them, the sampling-based algorithm can be used in both static and dynamic environments, with high time efficiency. The Rapidly-exploring Random Tree (RRT) algorithm [19] is one of the active sampling-based algorithms which is well-known for its fast convergence in multidimensional environments. However, the RRT algorithm has the shortcoming that it cannot guarantee an optimal path. To overcome this shortcoming, the RRT* algorithm [20] has been proposed. In the RRT* algorithm, an asymptotic optimal path can be reached through sufficient iterations by adding a routine to update the tree considering the path cost. However, its slow convergence rate became another issue. The RRT*-smart [21] algorithm was proposed to improve this weakness by accelerating the convergence rate to the asymptotic optimal path using intelligent sampling. In addition, the P-RRT* [22] algorithm with a potential-guided sampling technique was proposed to increase the convergence rate for the initial path. There are many other recent approaches to improve performance and overcome shortcomings of the RRT-based algorithms [23–28]. However, analyzing and applying all these algorithms requires a high excessive workload. Therefore, the P-RRT*-smart algorithm is selected and applied which is a fusion of classical P-RRT* and RRT*-smart to cover the applicability of a wide range of the path planning algorithms.

The following additional approaches are also applied when planning the terrain flight path. Areas over a certain distance from the surface are treated as obstacles. To do so, the generated path is always located near the surface. In addition, the cost due to threats between two nodes C_{threat} is calculated as follows:

$$\begin{aligned} C_{threat} &= \sum_{j=1}^{N_{step}} \Delta C_{threat,j} \\ \Delta C_{threat} &= \sum_{i=1}^{N_{threat}} f_{threat,i}(R_i, R_{\max,i}, s_{threat,i}, \varepsilon_{r,i}) \end{aligned} \tag{3}$$

where N_{threat} is the total number of threats in the environment and N_{step} is the total number of steps between two nodes. In Equation (3), the step cost ΔC_{threat} in each step is calculated using the cost function presented in Equation (1) while advancing between nodes by the prescribed step size. By summing all the calculated step costs, the cost due to threats between the nodes can be calculated. Since the cost due to threats continues to add up while the aircraft is within the threat range (i.e., $R_i < R_{\max,i}$), it is possible to account for the cost change depending on the flight time consumed within the threat range. A geometrical schematic of the step cost concept at an arbitrary j-th step between two nodes in the presence of two existing threats is shown in Figure 3.

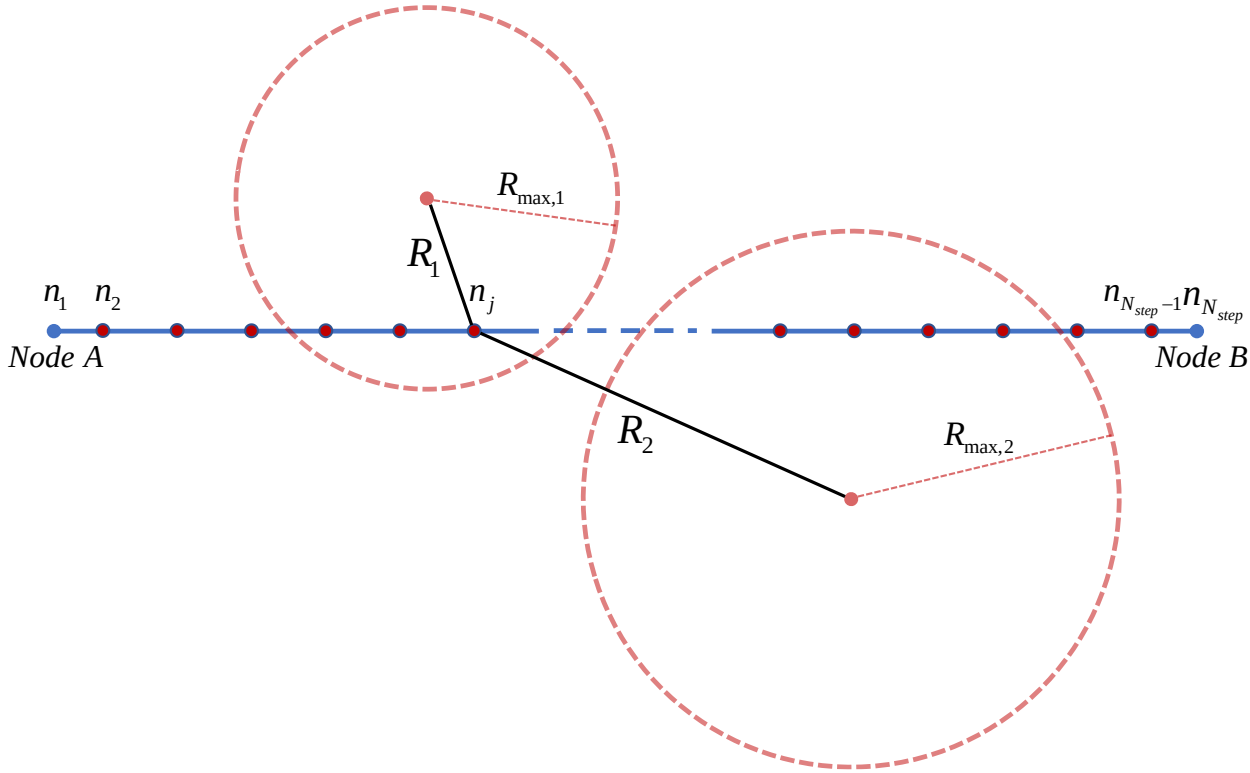

Figure 3. Geometrical schematic of the step cost concept.

The node-to-node cost C_{n2n} can then be calculated by additionally considering the distance cost between nodes as:

$$\begin{aligned} C_{n2n} &= C_{dist} + C_{threat} \\ C_{dist} &= \|\boldsymbol{r}_A - \boldsymbol{r}_B\| \end{aligned} \tag{4}$$

where $\boldsymbol{r}_A$ and $\boldsymbol{r}_B$ are the position vectors of nodes A and B, respectively.

Figure 4 represents an example case of terrain path planning. The path planning and all the other simulations are performed by Visual Fortran, Window 10 home, with the help of Intel Core i7-6700K CPU (4.0 GHz) with 32 GB of RAM. The total running time is 2.251 s with the 5000 total number of samplings. However, both the initial path convergence and the optimal path convergence times are quite short, 0.096 s and 0.7344 s, respectively. As shown in Figure 4a, the planned path avoids a threat with relatively strong strength to minimize the path cost. In addition, the planned path is generated within 100 m of the vertical distance from the surface as shown in Figure 5.

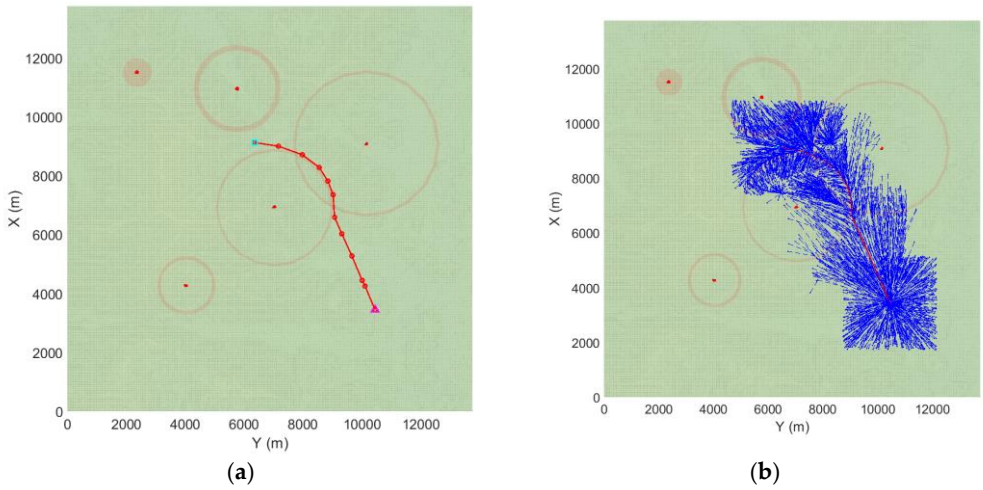

Figure 4. An example of terrain path planning: on map (**a**) Planned path; (**b**) Generated tree.

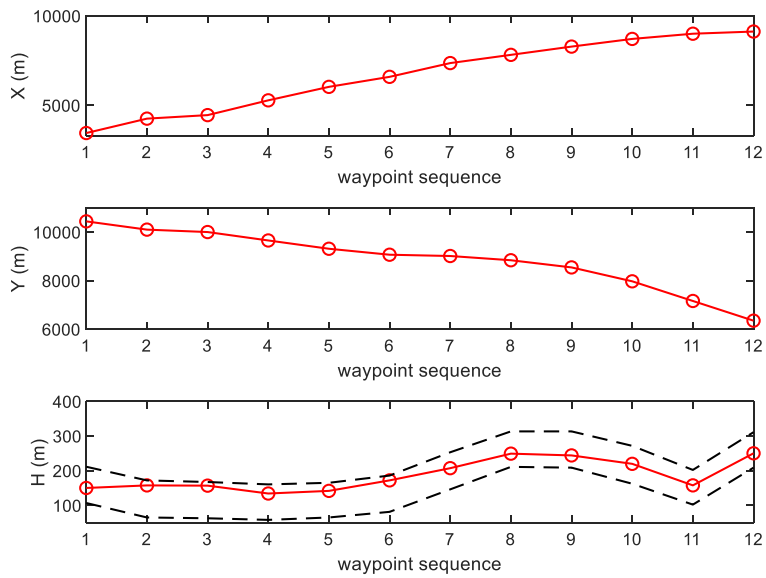

Figure 5. An example of terrain path planning: Graph.

4. Shortest Target Intercept Path Planner

The target areas are likely to be interspersed with threats that take hostile actions. To increase the chances of completing a successful mission, the aircraft must survive during the intercept process. Accordingly, it is necessary to generate the shortest distance path from the vicinity of the target area so that the mission can be carried out as quickly as possible. Furthermore, in order to attack the target point, the aircraft's heading angle should be aligned with the target point before the action takes place. Considering two necessary conditions, the Dubins circle can provide reliable results. Dubins [29] presented a method to generate the shortest path to reach the final position and heading while satisfying the constraint that vehicles must move along the arcs of a minimal turning radius $R_{Turning}$ while proceeding in the initially prescribed heading. The path generated by this approach may not be an obstacle-free path, and therefore can only be used in an environment undisturbed by obstacles. However, this approach is useful since it can generate a simple and fast flyable path. Based on this advantage, a planner was designed to plan the path of the target intercept mission element.

The concept of a target intercept path planning strategy is shown in Figure 6. First, the position and entry angle of the target and position and heading angle of the UCAV is prescribed. Furthermore, the height of the intercept mission plane is set to an XY plane

high enough from the highest terrain height in the intercept mission area. The UCAV aims at the target while flying straight in the direction of the given entry angle ψ_e. Thus, the aiming start position and weapon release point are defined as points separated by certain distances d_{Aiming} and $d_{Release}$ in the direction of the entry angle from the target. Next, the path is generated by connecting the initial position of the UCAV, the aiming start position, and the weapon release point based on the Dubins path concept [30]. The same process is repeated until the path is generated which intercepts all the targets. Finally, the rest of the path is generated with the prescribed exit point and exit angle from the last target location. In this concept, $R_{Turning}$ can be determined by the aircraft's dynamic characteristics and speed, and d_{Aiming}, $d_{Release}$ can be determined by the missile's aiming capability.

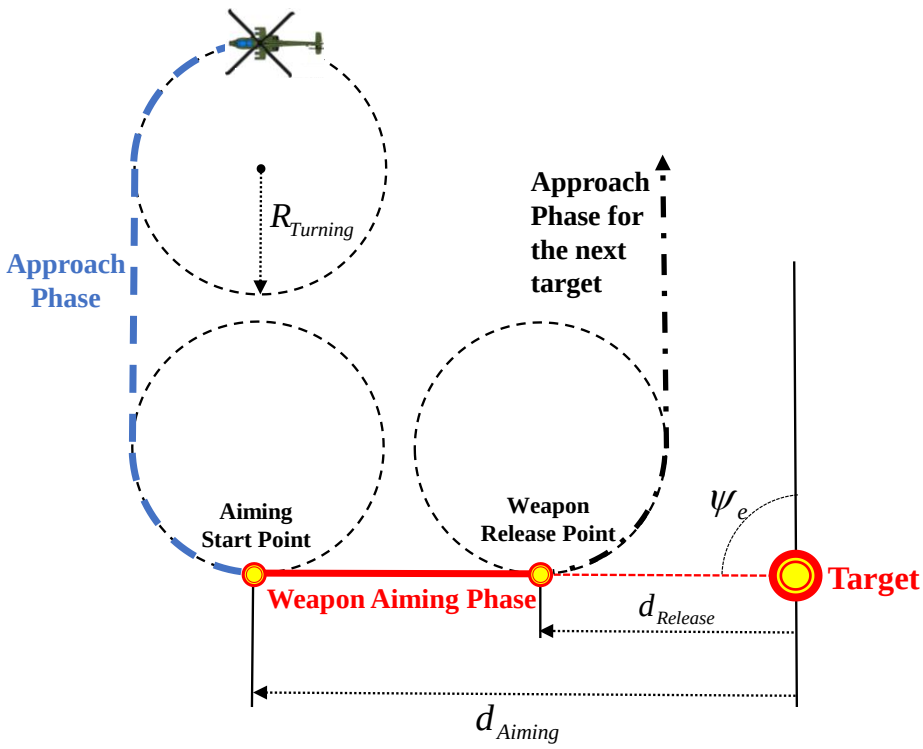

Figure 6. Target intercept path planning strategy.

The length of the path generated by the presented process varies according to the intercept entry angles and the target intercept sequence. Therefore, the entry angles are needed to be optimized to obtain the shortest path. The optimization problem can be formulated as Equation (5). The object function f_{obj} is the total length of the generated path and the design variables $\boldsymbol{\psi}_e$ are the intercept entry angles of each target. The formulated problem can be solved using an NLP solver and the robust SQP method [31] is applied in this paper.

$$\min_{\boldsymbol{\psi}_e} f_{obj}(\boldsymbol{\psi}_e), \ \boldsymbol{\psi}_e = [\psi_{e,1}, \psi_{e,2}, \cdots, \psi_{e,n}] \in \mathbb{R}^n \tag{5}$$

However, the target intercept sequence is another factor that determines the length of the path. Accordingly, the target intercept sequence in which the path length is minimized should be determined. Therefore, optimization is performed on all possible combinations of target intercept sequences, and a combination having the shortest path length is selected.

Figure 7 illustrates an example case of the proposed planner. The square points represent the location of the targets. Furthermore, each of the parameters d_{Aiming}, $d_{Release}$, and $R_{Turning}$ were set to 300 m, 100 m, and 300 m, respectively. The solid line represents the planned path, and the dash lines describe the turning radius. The total consumed time to optimizing was 3.524 s. Figure 7 shows that the target entry angles, and target intercept sequence are properly optimized.

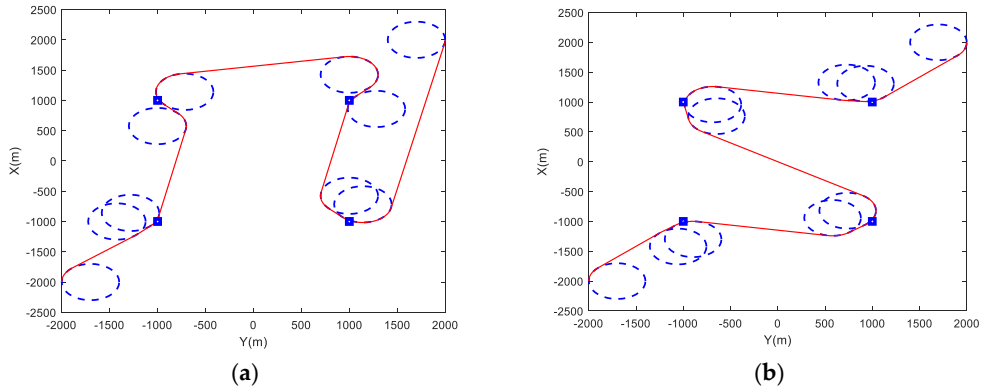

Figure 7. An example of target intercept path planning: (**a**) Initial path; (**b**) Optimized path

The computation time seems unsuitable for real-time computation. However, this time is the time it takes when optimization is performed with the initial value set to 0 for all possible intercept sequences. When in flight, a strategy of updating the path in real-time can be taken while setting the initial value to the previously optimized value and performing optimization for a single intercept sequence. To validate this strategy, optimization was performed by changing each target position shown in Figure 7 by 100 m, setting the previously optimized entry angles to the initial values, and performed for the previously optimized intercept sequence. The time required for optimization was 0.2190 s, confirming the possibility of real-time application.

5. Application on Mission Scenarios

ASMs consist of AI, CAS, SEAD, and AO missions depending on the mission environment and its goal. The major differences between these four missions are the density and distribution of threats on the environment and the property of the targets.

First, in the environmental perspective view, AI and AO missions require the UCAVs to penetrate deep into the enemy territory. Therefore, there is a possibility of many scattered threats along UCAVs' path. In SEAD missions, most targets are located on highlands since air defense assets are already deployed. CAS missions generally aim to strike targets located on the border between enemy and friendly territories where the number of threats increases when approaching the target intercept area.

Second, in the target property perspective view, all hostile assets can be targeted in counterland missions, including the enemy's military potential, whereas only enemy air defense assets are targeted in counterair missions. However, there is no difference when planning the path of the two missions since there is a commonality that the targets are located on the surface. For this reason, the proposed planner validation for AI, AO, and CAS missions can be performed together in a single mission scenario. Considering that the targets of the SEAD mission are located on the highlands, another mission scenario is also constructed.

5.1. AI Mission Scenario

The targets in the AI mission scenario are shown in Figure 8 with the detailed location coordinates are represented in Table 2. The targets are assumed to be parked enemy vehicles.

Figure 9 illustrates the planned path of the AI mission scenario. The red transparent spherical area represents randomly placed threats, and the transparent cube area represents the target intercept mission area. The mission proceeds in order, starting with the triangle point and passing through the square point, the pentagonal point, and the hexagonal point, while the exact coordinates are shown in Table 3. The targets are represented by x points and the threat properties are shown in Table 4.

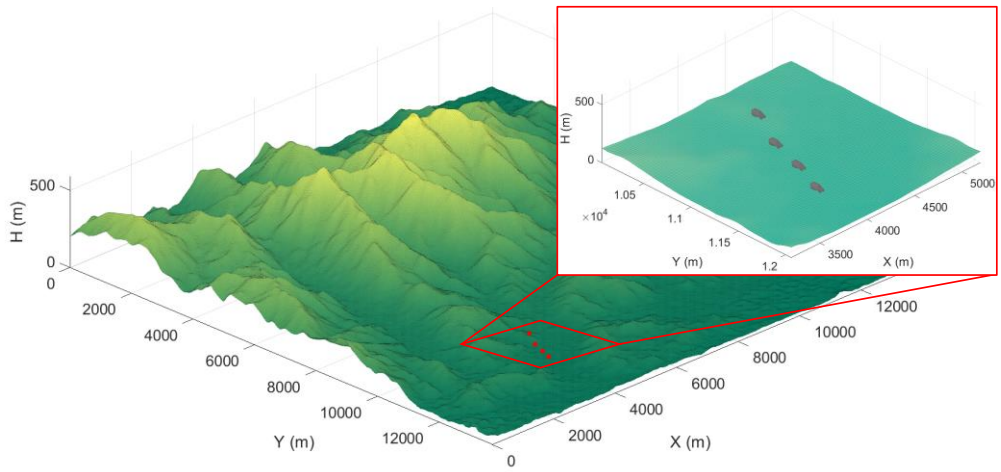

Figure 8. Targets for AI mission.

Table 2. Targets' coordinate of the AI mission scenario.

Target Number	X Position (m)	Y Position (m)	H Position (m)
Target #1	4438.0	10,520.0	69.53
Target #2	4250.0	10,890.0	46.35
Target #3	4143.0	11,240.0	41.72
Target #4	4008.0	11,570.0	41.72

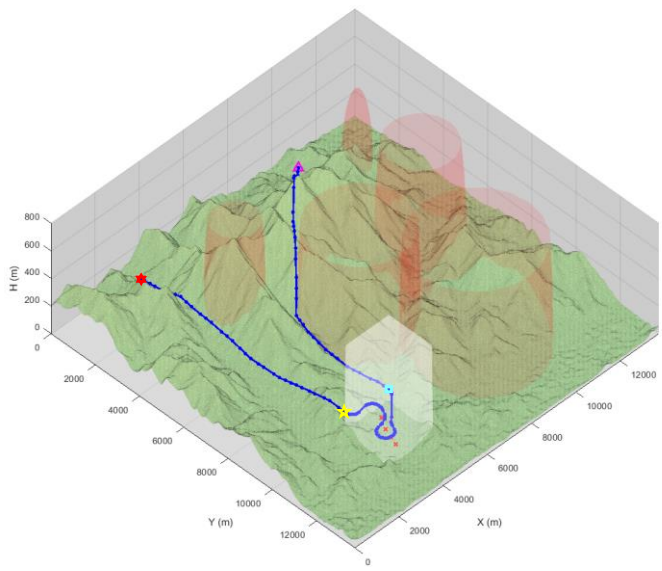

Figure 9. Planned path of the AI mission scenario.

Table 3. SEAD mission scenario's waypoint locations.

Waypoints	X Position (m)	Y Position (m)	H Position (m)
Triangle Point	10,250.0	941.5	150.0
Square Point	5196.0	10,060.0	147.9
Pentagonal Point	3196.0	10,060.0	212.8
Hexagonal Point	3120.0	941.5	150.0

Table 4. Threats' properties of the AI mission scenario.

Threat Number	X Position (m)	Y Position (m)	H Position (m)	Strength of the Threat	Maximum Radius of the Threat (m)
Threat #1	10,950.0	5756.0	69.53	30.0	1500.0
Threat #2	9092.0	10,140.0	58.0	50.0	2500.0
Threat #3	4277.0	4035.0	322.2	50.0	1000.0
Threat #4	6913.0	7021.0	213.2	100.0	2000.0
Threat #5	11,490.0	2367.0	245.7	10.0	500.0

The total consumed time is 30.6 s, and the number of samplings is set as 5000 for each terrain flight path planning for AI mission planning. As shown in Figure 9, the path is appropriately generated to avoid the threats while intercepting targets with the shortest length. Furthermore, the path is generated within 100 m above the surface in the terrain flight phase.

5.2. SEAD Mission Scenario

Figure 10 shows the targets of the SEAD mission scenario. The targets are assumed as already deployed enemy air defense assets on the highlands. The total number of targets is four and the locations of the targets are shown in Table 5.

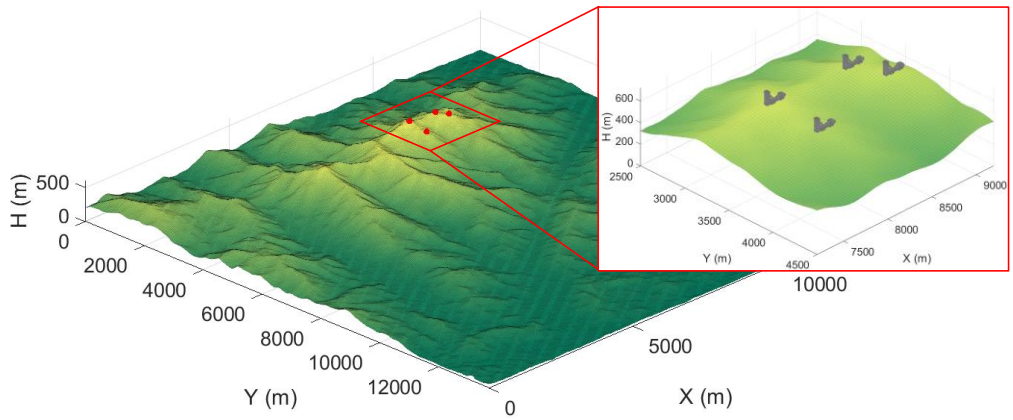

Figure 10. Targets for the SEAD mission scenario.

Table 5. Targets' coordinate of the SEAD mission scenario.

Target Number	X Position (m)	Y Position (m)	H Position (m)
Target #1	8850.0	3255.0	563.0
Target #2	9011.0	3551.0	561.0
Target #3	7962.0	3255.0	592.0
Target #4	8043.0	3739.0	510.0

Figure 11 represents the planned path of the SEAD mission scenario. The red transparent spherical area represents randomly placed threats, and the transparent cube area represents the target intercept mission area. The mission proceeds in the following order: the triangle point, the square point, the pentagonal point, and the hexagonal point while the exact coordinates are shown in Table 6. The targets are represented by x points and the threats' properties are shown in Table 7.

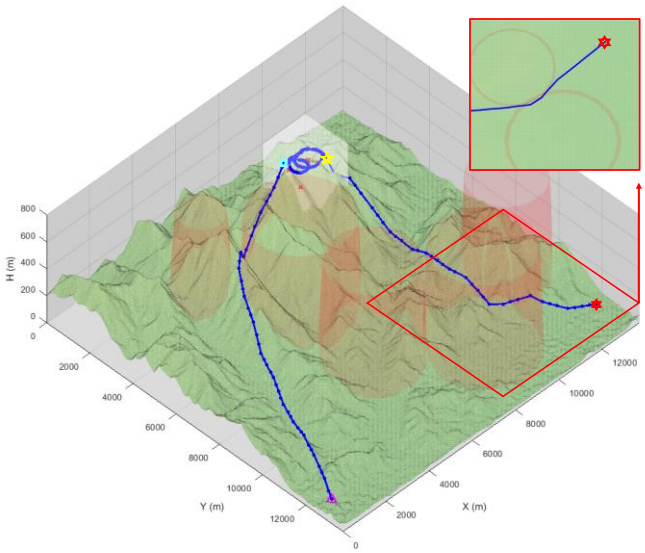

Figure 11. Planned path of the SEAD mission scenario.

Table 6. SEAD mission scenario's waypoint locations.

Waypoints	X Position (m)	Y Position (m)	H Position (m)
Triangle Point	618.7	12,590.0	41.72
Square Point	7800.0	3200.0	667.0
Pentagonal Point	9800.0	3200.0	474.7
Hexagonal Point	12,910.0	12,590.0	100.0

Table 7. Threats' properties of the SEAD mission scenario.

Threat Number	X Position (m)	Y Position (m)	H Position (m)	Strength of the Threat	Maximum Radius of the Threat (m)
Threat #1	11,920.0	9415.0	306.0	200.0	1500.0
Threat #2	9092.0	11,140.0	58.0	100.0	2000.0
Threat #3	3685.0	3470.0	280.4	100.0	1000.0
Threat #4	5864.0	5918.0	204.0	200.0	2000.0
Threat #5	6052.0	9065.0	67.21	1000.0	1800.0

The total consumed time is 16.85 s, and the number of samplings is set as 5000 for each terrain flight path planning for SEAD mission planning. The path shown in Figure 11 avoids a threat with relatively strong strength near the hexagonal point. Furthermore, the path is generated within 100 m above the surface in the terrain flight phase. One can find that the highlighted path in Figure 11 goes between threat #1 and threat #2 while bypassing a greater threat. This result occurs when it is more cost-effective to go through a threat than to avoid it.

6. Trajectory Tracking Simulation

Simulation of the planned trajectory tracking is essential to confirm the practical applicability of the proposed algorithm. Therefore, simulations are performed to track the flight trajectory as a function of time generated based on the planned path.

The waypoints represented in Section 5 only contain the sequence of position vectors. However, the Flight Control System (FCS) which will be mentioned later, requires heading angle information as well as position vectors. Furthermore, this information must be given as a function of time. For these reasons, a series of processes of allocating time and heading angle to the waypoint and converting the path into functions of time is required. Arrival time at each waypoint is allocated by assuming that UCAV is flying in a straight line between each waypoint at a prescribed constant speed. Moreover, the heading angle

at each waypoint is assigned to face the next waypoint. Additional waypoints can be assigned to describe the original path more precisely where the waypoints can be expressed as a function of time through 7th-order spline interpolation [32]. The predicted arrival time may not be precise since the interpolated curve is not a straight line. To solve this problem, a simple iterative method is used to estimate the exact arc length and travel time simultaneously. Further details about trajectory generation are represented in Ref [33].

In order to design an appropriate trajectory tracking flight control system, trajectory tracking performance, robustness against disturbances and uncertainties, and the operating range of the aircraft must be considered. Incremental Backstepping Control (IBSC) guarantees stability across all Operational Flight Envelopes (OFE) based on the Lyapunov stability theory and is not affected by mismatched uncertainty. For this reason, there have been many approaches to design a controller based on the IBSC concept [34–40], and this paper also uses an IBSC-based tracking controller [33]. The reference trajectory was directly used as a feedback signal to obtain excellent tracking performance. For the completeness of this paper, the controller presented in Ref. [33] will be briefly described.

The main feature of the incremental control method is its stronger robustness compared to the conventional model-based control approaches. Rather than solely depending on the model dynamics, incremental controllers use the measurements of any aerodynamic changes through available sensors. Therefore, changes due to external disturbances or modeling errors can be measured and compensated directly to the controller, making the controller insensitive to such unfavorable effects. The aircraft's equation of motion and the kinematic relations are defined as follows:

$$\begin{array}{c} \dot{\boldsymbol{v}} = \frac{1}{m}\boldsymbol{f_b} - \boldsymbol{\omega} \times \boldsymbol{v} \\ \dot{\boldsymbol{\omega}} = \boldsymbol{J}^{-1}(\boldsymbol{m}_b - \boldsymbol{\omega} \times \boldsymbol{J}\boldsymbol{\omega}) \\ \boldsymbol{\omega} = \boldsymbol{L}\dot{\boldsymbol{\varphi}} \\ \boldsymbol{v} = \boldsymbol{C}\dot{\boldsymbol{r}} \end{array}, \ \boldsymbol{v} = \begin{pmatrix} u \\ v \\ w \end{pmatrix}, \boldsymbol{\omega} = \begin{pmatrix} p \\ q \\ r \end{pmatrix}, \boldsymbol{\varphi} = \begin{pmatrix} \phi \\ \theta \\ \psi \end{pmatrix}, \boldsymbol{r} = \begin{pmatrix} x \\ y \\ z \end{pmatrix} \tag{6}$$

where $\boldsymbol{v}$ and $\boldsymbol{\omega}$ represent linear and angular velocity vector with respect to the aircraft's body-fixed frame, $\boldsymbol{f}_b$ and $\boldsymbol{m}_b$ represent force and moment vector, and $\boldsymbol{r}$ and $\boldsymbol{\varphi}$ represent the position and attitude vector of the aircraft. Furthermore, $\boldsymbol{C}$ and $\boldsymbol{L}$ are represented using the definition of the trigonometric functions like $c_\alpha = \cos\alpha$ and $s_\alpha = \sin\alpha$ for $\alpha = \phi,\ \theta,\ \psi$ as.

$$\begin{array}{l} \mathbf{C} = \begin{pmatrix} c_\theta c_\psi & c_\theta s_\psi & -s_\theta \\ s_\phi s_\theta c_\psi - c_\phi s_\psi & s_\phi s_\theta s_\psi + c_\phi c_\psi & s_\phi c_\theta \\ c_\phi s_\theta c_\psi + s_\phi s_\psi & c_\phi s_\theta s_\psi - s_\phi c_\psi & c_\phi c_\theta \end{pmatrix} \\ \mathbf{L} = \begin{pmatrix} 1 & 0 & -s_\theta \\ 0 & c_\phi & c_\theta s_\phi \\ 0 & -s_\phi & c_\theta c_\phi \end{pmatrix} \end{array} \tag{7}$$

The second-order dynamics for $(\boldsymbol{r}, \boldsymbol{\varphi})$ are derived as:

$$\begin{array}{c} \ddot{\boldsymbol{r}} = \boldsymbol{C}^{-1}\left\{\frac{\boldsymbol{f}_b}{m} - \left(\boldsymbol{L}\dot{\boldsymbol{\varphi}}\right) \times \left(\boldsymbol{C}\dot{\boldsymbol{r}}\right) - \dot{\boldsymbol{C}}\dot{\boldsymbol{r}}\right\} \\ \ddot{\boldsymbol{\varphi}} = \boldsymbol{L}^{-1}\boldsymbol{J}^{-1}\left\{\boldsymbol{m}_b - \left(\boldsymbol{L}\dot{\boldsymbol{\varphi}}\right) \times \left(\boldsymbol{J}\boldsymbol{L}\dot{\boldsymbol{\varphi}}\right)\right\} - \boldsymbol{L}^{-1}\dot{\boldsymbol{L}}\dot{\boldsymbol{\varphi}} \end{array} \tag{8}$$

which can be represented as following second-order nonlinear equation:

$$\begin{array}{c} \ddot{\boldsymbol{x}} = f\left(\boldsymbol{x}, \dot{\boldsymbol{x}}, \boldsymbol{u}_p\right) \\ \boldsymbol{y} = \boldsymbol{x} \\ \boldsymbol{x} = (x, y, z, \phi, \theta, \psi)^T \\ \boldsymbol{u}_p = (\delta_0, \delta_{1C}, \delta_{1S}, \delta_{TR})^T \end{array} \tag{9}$$

where $\boldsymbol{u}_p$ is the primary control vector of a conventional helicopter consisting of the main rotor collective (δ_0), lateral-cyclic (δ_{1C}), longitudinal-cyclic (δ_{1S}), and tail rotor collective(δ_{TR}). Let us define the dynamics in Equation (9) represented at $t = t_0$ as:

$$\ddot{\boldsymbol{x}}_0 = \boldsymbol{f}_0 = \boldsymbol{f}(\boldsymbol{x}_0, \dot{\boldsymbol{x}}_0, \boldsymbol{u}_{p0}) \tag{10}$$

By applying the Taylor's series expansion to Equation (10) at $t = t_0 + \Delta t$, and assuming Δt is small enough, the incremental dynamics can be derived as:

$$\begin{aligned} \ddot{\boldsymbol{x}} &= \boldsymbol{f}(\boldsymbol{x}, \dot{\boldsymbol{x}}, \boldsymbol{u}_p) \\ &= \boldsymbol{f}(\boldsymbol{x}_0 + \Delta\boldsymbol{x}, \dot{\boldsymbol{x}}_0 + \Delta\dot{\boldsymbol{x}}, \boldsymbol{u}_{p0} + \Delta\boldsymbol{u}_p) \\ &\approx \boldsymbol{f}_0 + \frac{\partial \boldsymbol{f}_0}{\partial \boldsymbol{u}_p}\Delta\boldsymbol{u}_p + \underbrace{\frac{\partial \boldsymbol{f}_0}{\partial \boldsymbol{x}}\Delta\boldsymbol{x} + \frac{\partial \boldsymbol{f}_0}{\partial \dot{\boldsymbol{x}}}\Delta\dot{\boldsymbol{x}}}_{\text{Small } \Delta t\text{:Negligible}} \\ &= \boldsymbol{f}_0 + \boldsymbol{G}_n\Delta\boldsymbol{u}_p \end{aligned} \tag{11}$$

Since the rank the control effectiveness matrix $\boldsymbol{G}_n \in \mathbb{R}^{6\times4}$ is less than the dimension of the system output $\boldsymbol{y} \in \mathbb{R}^6$, the system is underactuated. To cope with such difficulty, the slack variable approach is adopted as in Ref. [29] as follows:

$$\ddot{\boldsymbol{x}} = \boldsymbol{f}_0 + \boldsymbol{G}\Delta\boldsymbol{u}_p + \Delta\boldsymbol{\xi} \tag{12}$$

where $\boldsymbol{G}$ and $\Delta\boldsymbol{\xi}$ are defined using the slack variable matrix $\boldsymbol{G}_s \in \mathbb{R}^{6\times2}$ and the slack variable vector $\Delta\boldsymbol{u}_s \in \mathbb{R}^2$ as:

$$\begin{aligned} \boldsymbol{G} &= (\boldsymbol{G}_n, \boldsymbol{G}_s) \\ \Delta\boldsymbol{\xi} &= -\boldsymbol{G}_s\Delta\boldsymbol{u}_s \end{aligned} \quad \Delta\boldsymbol{u} = \begin{pmatrix} \Delta\boldsymbol{u}_p \\ \Delta\boldsymbol{u}_s \end{pmatrix} \tag{13}$$

If $\boldsymbol{G}_s$ is selected to make $\boldsymbol{G}$ nonsingular, standard nonlinear control design methods can be applied to Equation (12).

The IBSC design starts by defining the trajectory tracking errors with the desired trajectory $\boldsymbol{x}_d$ as:

$$\begin{aligned} \boldsymbol{z}_1 &= \boldsymbol{x} - \boldsymbol{x}_d \\ \boldsymbol{z}_2 &= \dot{\boldsymbol{x}} - \boldsymbol{\alpha} \end{aligned} \tag{14}$$

where $\boldsymbol{\alpha}$ is the virtual control vector. Now, a control Lyapunov function V is defined.

$$V = \frac{1}{2}\boldsymbol{z}_1^T\boldsymbol{Q}\boldsymbol{z}_1 + \frac{1}{2}\boldsymbol{z}_2^T\boldsymbol{z}_2 + \frac{1}{2}\Delta\boldsymbol{\xi}^T\Gamma_{\xi}^{-1}\Delta\boldsymbol{\xi} > 0 \tag{15}$$

Without further derivation, the IBSC law that stabilizes the above Lyapunov function ($\dot{V} < 0$) can be selected as:

$$\begin{aligned} \boldsymbol{\alpha} &= -\boldsymbol{Q}^{-1}\boldsymbol{K}_1\boldsymbol{z}_1 + \dot{\boldsymbol{x}}_d \\ \Delta\boldsymbol{u} &= -\boldsymbol{G}^{-1}\left(\boldsymbol{K}_2\boldsymbol{z}_2 + \boldsymbol{Q}^{-T}\boldsymbol{z}_1 + \ddot{\boldsymbol{x}}_0 + \Delta\boldsymbol{\xi} - \dot{\boldsymbol{\alpha}}\right) \\ \Delta\dot{\boldsymbol{\xi}} &= \boldsymbol{\Gamma}_{\xi}\boldsymbol{z}_2 \end{aligned} \tag{16}$$

$$\dot{V} = -\boldsymbol{z}_1^T\boldsymbol{K}_1\dot{\boldsymbol{z}}_1 - \boldsymbol{z}_2^T\boldsymbol{K}_2\dot{\boldsymbol{z}}_2 < 0 \tag{17}$$

where, $\boldsymbol{Q} \in \mathbb{R}^{6\times6}$, $\boldsymbol{K}_1 \in \mathbb{R}^{6\times6}$, and $\boldsymbol{K}_2 \in \mathbb{R}^{6\times6}$ are diagonal, positive definite matrices composing controller gains, and $\boldsymbol{\Gamma}_{\xi} \in \mathbb{R}^{6\times6}$ is a diagonal, positive definite matrix composing updating law gains. If you need further details of the controller, referring to Ref [33] is recommended.

Rotorcrafts are more appropriate to perform low-flying contour chasing maneuvers than fixed-wing aircraft for their low-speed flyability. For this reason, the BO-105 helicopter nonlinear model, modeled using the HETLAS program [41,42], is utilized.

The trajectories are generated based on the AI mission and the SEAD mission paths in Section 5. Figures 12 and 13 represent the generated trajectories to fly at a constant speed of

40 m/s. The dashed line represents the height limit boundary of the terrain flight. That is, the lower boundary indicates the ground surface, and the upper boundary indicates a line of 100 m above the surface. As shown in Figure 12a, the height of the terrain flight trajectory was generated within 100 m from the surface. Meanwhile, the intercept maneuver trajectory was not affected the height constraint.

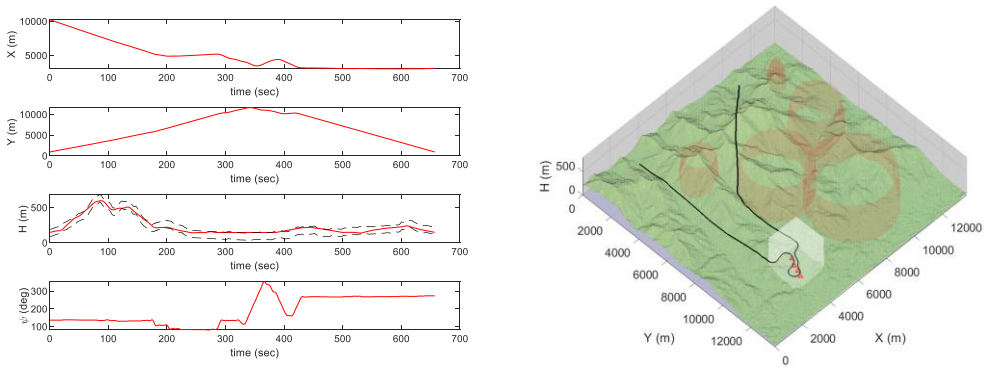

(**a**) (**b**)

Figure 12. Generated trajectory in the AI mission scenario: Trajectory (**a**) for time; (**b**) on 3D map.

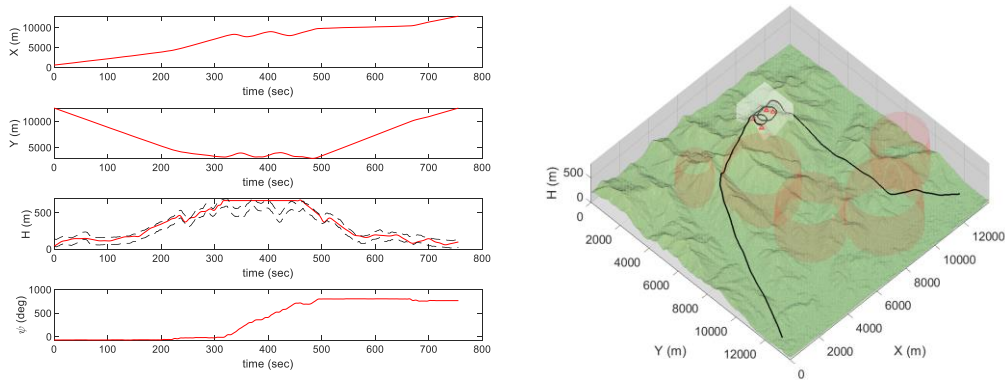

(**a**) (**b**)

Figure 13. Generated trajectory in the SEAD mission scenario: Trajectory (**a**) for time; (**b**) on 3D map.

Figures 14 and 15 show tracking results and its error. Both results represent highly accurate tracking performance while showing position error within 1 m and heading angle error within 0.2 degrees. Through such high-accuracy tracking performance, the terrain flight missions can be performed without any collision.

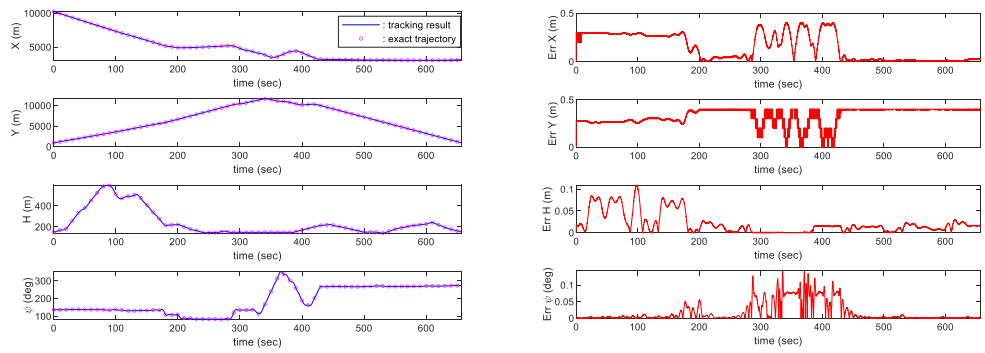

(**a**) (**b**)

Figure 14. Trajectory tracking result in the AI mission scenario: (**a**) Tracking result; (**b**) Tracking error.

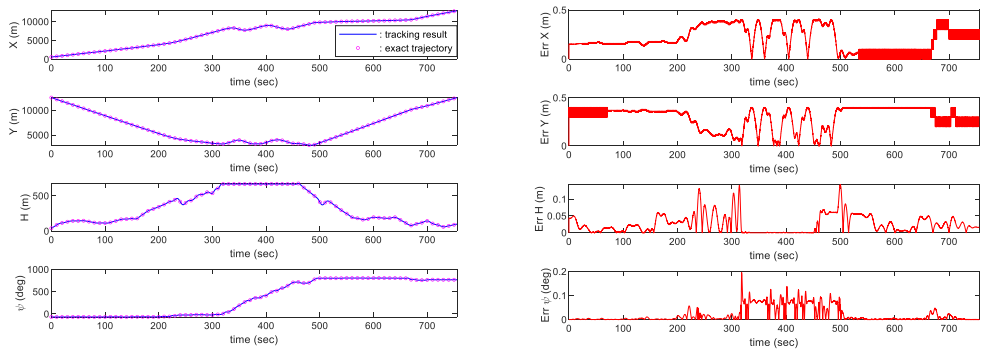

(**a**) (**b**)

Figure 15. Trajectory tracking result in the SEAD mission scenario: (**a**) Tracking result; (**b**) Tracking error.

The control inputs and states during the simulation are represented in Figures 16–18. In the AI mission scenario, the lateral velocity varies over 40 m/s at about 300 s. Furthermore, the roll attitude temporally reaches over −30 degrees during intercept maneuver flight and the variation over 10 degrees in the pitch angle is represented at about 300 s. In the SEAD mission scenario, the lateral velocity varies over 40 m/s at about 650 s. Moreover, the roll attitude temporally reaches over 20 degrees during intercept maneuver flight and the variation over −15 degrees in the pitch angle is represented at about 320 s. The results in both simulations prove that the presented controller can maintain continuous tracking performance even with the aggressive maneuver. Furthermore, SEAD missions can be successfully performed with large height variations, where the maximum rate of climb reaches more than 10 m/s and the minimum rate of climb reaches near −20 m/s. In addition, the result is visualized in Figures 19 and 20 to help discernible understanding.

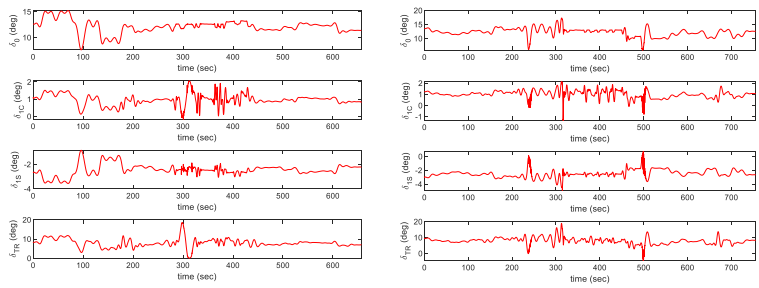

(**a**) (**b**)

Figure 16. Trajectory tracking result: control inputs for (**a**) the AI mission scenario; (**b**) for the SEAD mission scenario.

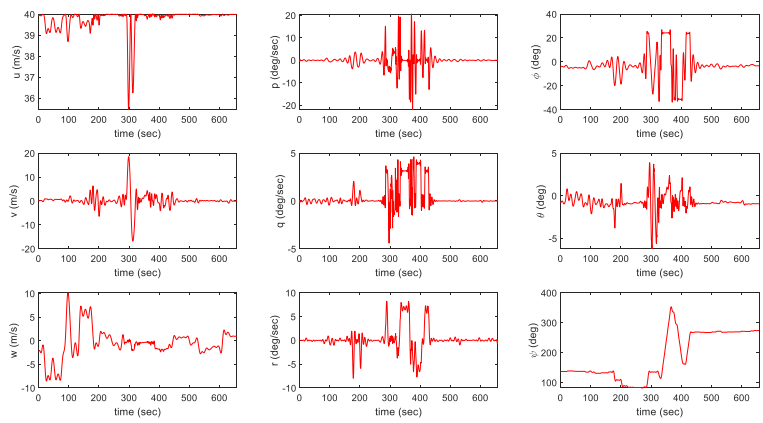

Figure 17. Trajectory tracking result in the AI mission scenario: states.

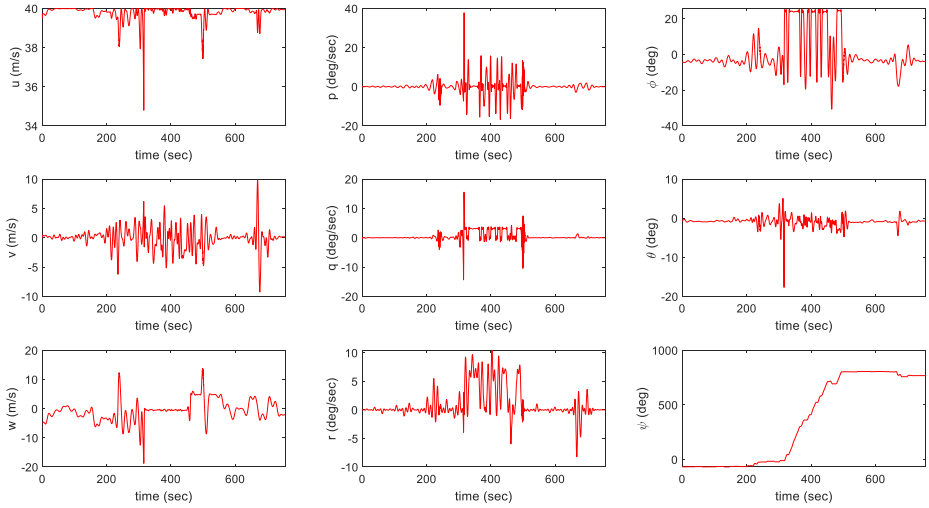

Figure 18. Trajectory tracking result in the AI mission scenario: states.

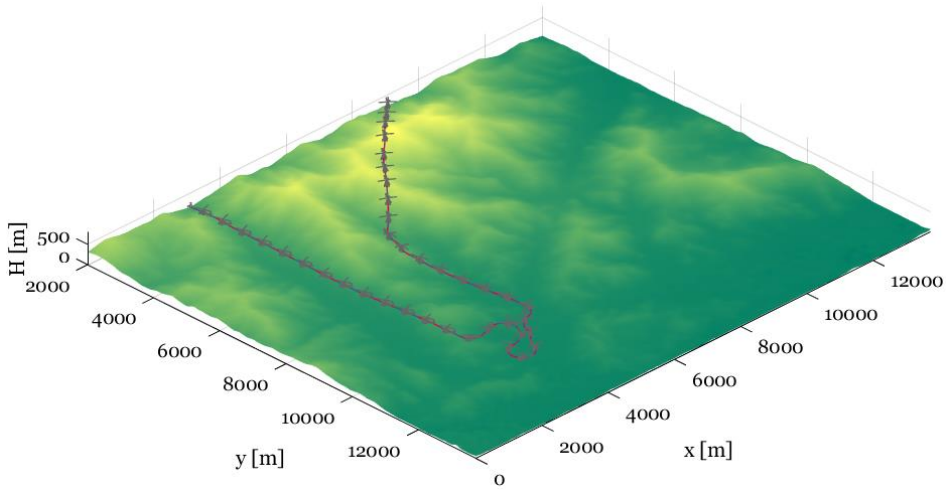

Figure 19. Trajectory tracking result in the AI mission scenario: visualization.

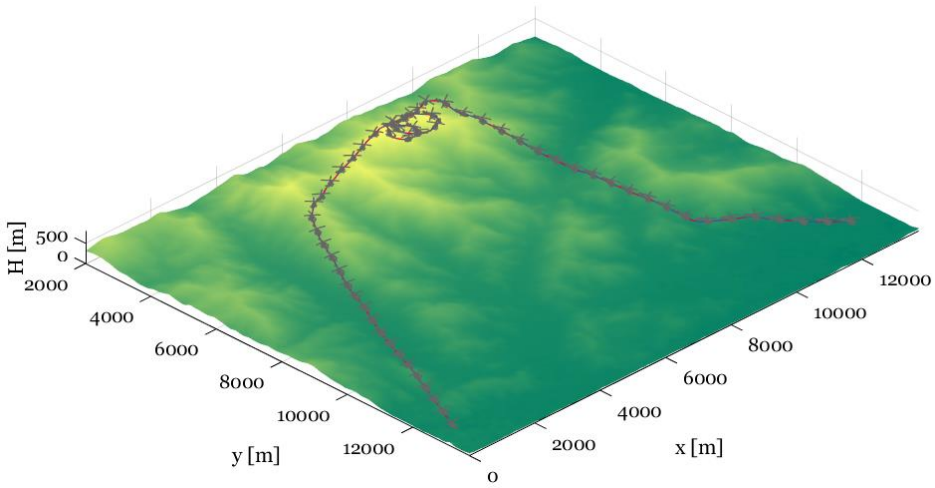

Figure 20. Trajectory tracking result in the SEAD mission scenario: visualization.

7. Conclusions

A mission planner that enables effective ASM performance while considering the risk factors of the mission environment has been proposed and validated in this paper. First, ASMs were considered to consist of three sequential mission elements. The P-RRT*-smart algorithm was used to plan the ingress and egress mission element paths to quickly find the asymptotic global optimal path. The algorithm made it possible to find a path that could fly within 100 m of the surface. In addition, the concept of step cost was developed to account for the threats spread in the mission area. In order to increase the survivability of the UCAV and properly attack multiple targets, Dubins path was adopted in the intercept phase to generate short distance path near targets, taking into account the aircraft's dynamic characteristics and the aiming capability of the mounted missiles. However, since the total length of the path still depends on target entry angles and the order of interception, the NLP was formulated to minimize the total length of the intercept path considering both the intercept entry angles and target intercept sequences. In return, the shortest intercept path could be obtained through the robust SQP. The integrated planner was then demonstrated in several test scenarios using a 3D terrain model with randomly placed threats. Finally, tracking simulations of the given path were successfully performed through a nonlinear rotorcraft model, confirming the method's effectiveness.

Although the proposed planner has been confirmed to be an effective approach, questions about its real-time applicability remain. Therefore, there are several possible directions for the real-time applicability of this method. Since the proposed terrain path planner focuses on global planning, many samplings were performed in order to obtain the asymptotic optimal path. For this reason, the time consumed it takes to plan the terrain flight path shown in the results may seem quite long. In fact, the convergence time to the initial path and the optimal path was extremely short with in a few seconds. This characteristic shows the possibility of improvement as a real-time local planner sufficiently with a little improvement. The real-time local planner is focused on avoiding dynamic obstacles and threats during missions. To perform this task, the RT-RRT* [43] which is advanced for real-time application can be applied to the proposed planner. Furthermore, PQ-RRT [26] and bidirectional approaches [44] may also be useful to accelerate the convergence rate. Additionally, Line-of-Sight Path Optimization (LoSPO) technique [33] is a preferable option as a strategy to shorten the convergence time to the optimal path. Likewise, other RRT-based approaches can be applied to further improve the algorithm for real-time local planners.

The shortest intercept path planning may seem unsuitable for real-time applications. However, the time consumed shown in the results is the time required for optimization by setting the initial values to 0. In this case, it may take a long time to converge. Therefore, a strategy of planning the path with the previously optimized value as the initial value during the flight may be effective.

The results show that the proposed planner can generate the optimal path to approach the targets and the shortest path to intercept targets on the 3D global map which is the major difference from the previous studies. Furthermore, the presented simulation results show that the applied controller tracks the planned trajectory with high tracking performance, which proves that the generated trajectories from the proposed planner are flyable. In addition, the robust controller is adopted to cope with uncertainties such as the instantaneous weight reduction that occurs during an armed drop. Therefore, the method proposed in this paper can greatly contribute to planning air-to-surface missions of autonomous UCAVs.

Author Contributions: Supervision, C.-J.K.; Validation, J.-Y.A.; Writing—original draft, J.-W.W.; Writing—review & editing, Y.-S.C. All authors have read and agreed to the published version of the manuscript.

Funding: This research received no external funding.

Institutional Review Board Statement: Not available.

Informed Consent Statement: Not available.

Data Availability Statement: Not available.

Acknowledgments: This paper was written as part of Konkuk University's research support program for its faculty on sabbatical leave in 2021. Furthermore, this research was supported by Basic Science Research Program through the National Research Foundation of Korea(NRF) funded by the Ministry of Education(No. 2020R1A6A1A03046811).

Conflicts of Interest: The authors declare no conflict of interest.

Nomenclature

R	Radial distance
$R_{\max}$	Radial distance of maximum threat reach
f_{threat}	Function of threat distribution in the inner domain of threat
ε_r	RBF shape factor
s_{threat}	Strength of threat
$\varphi(*,*)$	Radial basis function
C_{threat}	Cost due to threats
C_{dist}	Distance cost
C_{n2n}	Node-to-node cost
ψ_e	Target intercept entry angle
d_{Aiming}	Distance from target to aiming point
$d_{Release}$	Distance from target to weapon release point
$R_{Turning}$	Turning radius
f_{obj}	Objective function
$\boldsymbol{\psi_e}$	vector of target intercept entry angles
$\boldsymbol{z}_1$	Position tracking error
$\boldsymbol{z}_2$	Velocity tracking error
$\boldsymbol{x}_d$	Desired trajectory
UCAV	Unmanned Combat Aerial Vehicles
ASM	Air-to-Surface Mission
SEAD	Suppression to Enemy Air Defenses
AI	Air Interdiction
CAS	Close Air Support
AO	Attack Operations
RRT	Rapidly exploring Random Tree
RBF	Radial Basis Function
NLP	Nonlinear Programming
SQP	Sequential Quadratic Programming
IBSC	Incremental Backstepping Control
OFE	Operational Flight Envelope
HETLAS	Helicopter Trim Linearization and Simulation

References

1. Beard, R.W.; McLain, T.W.; Goodrich, M.A.; Anderson, E.P. Coordinated target assignment and intercept for unmanned air vehicles. *IEEE Trans. Robot. Autom.* **2002**, *18*, 911–922. [CrossRef]
2. Eun, Y.; Bang, H. Cooperative control of multiple UCAVs for suppression of enemy air defense. In Proceedings of the AIAA 3rd 'Unmanned Unlimited' Technical Conference, Workshop and Exhibit, Chicago, IL, USA, 20–23 September 2004; Volume 20–23, pp. 1–14.
3. Triharminto, H.H.; Adji, T.B.; Setiawan, N.A. Dynamic uav path planning for moving target intercept in 3D. In Proceedings of the IEEE 2nd International Conference on Instrumentation Control and Automation, Shiraz, Iran, 27–29 December 2011; Volume 15–17, pp. 157–161. [CrossRef]
4. Shanmugavel, M.; Tsourdos, A.; White, B.; Zbikowski, R. Co-operative path planning of multiple UAVs using Dubins paths with clothoid arcs. *Control Eng. Pract.* **2010**, *18*, 1084–1092. [CrossRef]
5. Manyam, S.G.; Casbeer, D.; Von Moll, A.; Fuchs, Z. Optimal dubins paths to intercept a moving target on a circle. *Proc. Am. Control Conf.* **2019**, *2019*, 828–834. [CrossRef]
6. Zheng, Y.; Chen, Z.; Shao, X.; Zhao, W. Time-optimal guidance for intercepting moving targets by Dubins vehicles. *Automatica* **2021**, *128*, 109557. [CrossRef]

7. Ridder, J.P.; HandUber, J.C. Mission planning for joint suppression of enemy air defenses using a genetic algorithm. In Proceedings of the Genetic and Evolutionary Computation Conference, GECCO 2005, Washington, DC, USA, 25–29 June 2005; pp. 1929–1936. [CrossRef]
8. Griggs, B.J.; Parnell, G.S.; Lehmkuhl, L.J. An air mission planning algorithm using decision analysis and mixed integer programming. *Oper. Res.* **1997**, 662–676. [CrossRef]
9. Lan, Y. Multiple mobile robot cooperative target intercept with local coordination. *CCDC* **2012**, *2012*, 145–151.
10. Sharma, A.; Shoval, S.; Sharma, A.; Pandey, J.K. Path Planning for Multiple Targets Interception by the Swarm of UAVs based on Swarm Intelligence Algorithms: A Review. *IETE Tech. Rev. (Institution Electron. Telecommun. Eng. India)* **2021**, *0*, 1–23. [CrossRef]
11. Zhong, M.; Yang, R.N.; Wu, J.; Zhang, H. Multi-Target Strike Path Planning Based on Improved Decomposition Evolutionary Algorithm. *Math. Probl. Eng.* **2019**, *2019*, 7205154. [CrossRef]
12. Wu, W.; Wang, X.; Cui, N. Fast and coupled solution for cooperative mission planning of multiple heterogeneous unmanned aerial vehicles. *Aerosp. Sci. Technol.* **2018**, *79*, 131–144. [CrossRef]
13. Huang, H.; Zhuo, T. Multi-model cooperative task assignment and path planning of multiple UCAV formation. *Multimed. Tools Appl.* **2019**, *78*, 415–436. [CrossRef]
14. Baspinar, B.; Koyuncu, E. Survivability Based Optimal Air Combat Mission Planning with Reinforcement Learning. In Proceedings of the 2018 IEEE Conference on Control Technology and Applications, CCTA 2018, Copenhagen, Denmark, 21–24 August 2018; pp. 664–669. [CrossRef]
15. U.S Airforce. U.S Air Force Doctrine, AFDP 3-01, Counterair Operations. Available online: https://www.doctrine.af.mil/Doctrine-Publications/AFDP-3-01-Counterair-Ops/ (accessed on 5 July 2021).
16. U.S Airforce. U.S Air Force Doctrine, AFDP 3-03, Counterland Operations. Available online: https://www.doctrine.af.mil/Doctrine-Publications/AFDP-3-03-Counterland-Ops/ (accessed on 5 July 2021).
17. Morse, B.S.; Yoo, T.S.; Rheingans, P.; Chen, D.T.; Subramanian, K.R. Interpolating implicit surfaces from scattered surface data using compactly supported radial basis functions. In Proceedings of the International Conference on Shape Modeling and Applications, SMI 2001, Genova, Italy, 7–11 May 2001; pp. 89–98. [CrossRef]
18. Yang, L.; Qi, J.; Song, D.; Xiao, J.; Han, J.; Xia, Y. Survey of Robot 3D Path Planning Algorithms. *J. Control Sci. Eng.* **2016**, *2016*, 22. [CrossRef]
19. LaValle, S.M. Rapidly-Exploring Random Trees: A New Tool for Path Planning. Report No. TR 98-11, Computer Science Department, Iowa State University. 1998. Available online: http://janowiec.cs.iastate.edu/papers/rrt.ps (accessed on 5 July 2021).
20. Karaman, S.; Frazzoli, E. Sampling-based algorithms for optimal motion planning. *Int. J. Robot. Res.* **2011**, *30*, 846–894. [CrossRef]
21. Nasir, J.; Islam, F.; Malik, U.; Ayaz, Y.; Hasan, O.; Khan, M.; Muhammad, M.S. RRT*-SMART: A rapid convergence implementation of RRT*. *Int. J. Adv. Robot. Syst.* **2013**, *10*, 299–310. [CrossRef]
22. Qureshi, A.H.; Ayaz, Y. Potential functions based sampling heuristic for optimal path planning. *Auton. Robot.* **2016**, *40*, 1079–1093. [CrossRef]
23. Wang, J.; Meng, M.Q.H.; Khatib, O. EB-RRT: Optimal Motion Planning for Mobile Robots. *IEEE Trans. Autom. Sci. Eng.* **2020**, *17*, 2063–2073. [CrossRef]
24. Zhang, S.; Xu, T.; Cheng, H.; Liang, F. Collision Avoidance of Fixed-Wing UAVs in Dynamic Environments Based on Spline-RRT and Velocity Obstacle. In Proceedings of the IEEE 2020 International Conference on Unmanned Aircraft Systems, ICUAS, Athens, Greece, 1–4 September 2020; Volume 2020, pp. 48–58. [CrossRef]
25. Jeong, I.B.; Lee, S.J.; Kim, J.H. Quick-RRT*: Triangular inequality-based implementation of RRT* with improved initial solution and convergence rate. *Expert Syst. Appl.* **2019**, *123*, 82–90. [CrossRef]
26. Li, Y.; Wei, W.; Gao, Y.; Wang, D.; Fan, Z. PQ-RRT*: An improved path planning algorithm for mobile robots. *Expert Syst. Appl.* **2020**, *152*, 113425. [CrossRef]
27. Chiang, H.T.L.; Hsu, J.; Fiser, M.; Tapia, L.; Faust, A. RL-RRT: Kinodynamic Motion Planning via Learning Reachability Estimators from RL Policies. *IEEE Robot. Autom. Lett.* **2019**, *4*, 4298–4305. [CrossRef]
28. Wang, J.; Chi, W.; Li, C.; Wang, C.; Meng, M.Q.H. Neural RRT$*$: Learning-Based Optimal Path Planning. *IEEE Trans. Autom. Sci. Eng.* **2020**, *17*, 1748–1758. [CrossRef]
29. Dubins, L.E. On Curves of Minimal Length with a Constraint on Average Curvature, and with Prescribed Initial and Terminal Positions and Tangents. *Am. J. Math.* **1957**, *79*, 497. [CrossRef]
30. Lugo-Cardenas, I.; Flores, G.; Salazar, S.; Lozano, R. Dubins path generation for a fixed wing UAV. In Proceedings of the 2014 International Conference on Unmanned Aircraft Systems, ICUAS, Orlando, FL, USA, 27–30 May 2014; Volume 79, pp. 339–346. [CrossRef]
31. Kim, C.J.; Sung, S.; Shin, K.C. Pseudo-spectral application to nonlinear optimal trajectory generation of a rotorcraft. *Adv. Sci. Lett.* **2012**, *9*, 204–209. [CrossRef]
32. Kim, C.J.; Lee, D.H.; Hur, S.W. Efficient and Robust Inverse Simulation Techniques Using Pseudo-Spectral Integrator with Applications to Rotorcraft Aggressive Maneuver Analyses. *Int. J. Aeronaut. Sp. Sci.* **2019**, *20*, 768–780. [CrossRef]
33. Woo, J.W.; An, J.; Cho, M.G.; Kim, C. Integration of path planning, trajectory generation and trajectory tracking control for aircraft mission autonomy. *Aerosp. Sci. Technol.* **2021**, *1*, 107014. [CrossRef]
34. Wang, X.; van Kampen, E.J. Incremental Backstepping Sliding Mode Fault-Tolerant Flight Control. In Proceedings of the AIAA Scitech 2019 Forum, San Diego, CA, USA, 7–11 January 2019; Volume 118, p. 107014. [CrossRef]

35. Jeon, B.J.; Seo, M.G.; Shin, H.S.; Tsourdos, A. Understandings of incremental backstepping controller considering measurement delay with model uncertainty. *Aerosp. Sci. Technol.* **2021**, *109*, 106408. [CrossRef]
36. van Gils, P.; van Kampen, E.; de Visser, C.C.; Chu, Q.P. Adaptive Incremental Backstepping Flight Control for a High-Performance Aircraft with Uncertainties. In Proceedings of the AIAA Guidance, Navigation, and Control Conference, San Diego, CA, USA, 4–8 January 2016; Volume 118, p. 107014. [CrossRef]
37. Cho, M.G.; Jung, U.; An, J.-Y.; Choi, Y.-S.; Kim, C.-J. Adaptive Trajectory Tracking Control for Rotorcraft Using Incremental Backstepping Sliding Mode Control Strategy. *Int. J. Aerosp. Eng.* **2021**, *2021*, 1–15. [CrossRef]
38. Cordeiro, R.A.; Azinheira, J.R.; Moutinho, A. Cascaded Incremental Backstepping Controller for the Attitude Tracking of Fixed-Wing Aircraft. In Proceedings of the 5th CEAS Conference on Guidance, Navigation and Control, Milano, Italy, 3–5 April 2019.
39. Guerreiro, N.M.; Moutinho, A. Robust incremental backstepping controller for the attitude and airspeed tracking of a commercial airplane. In Proceedings of the 2019 IEEE 10th International Conference on Mechanical and Aerospace Engineering, ICMAE 2019, Brussels, Belgium, 22–25 July 2019; pp. 607–611. [CrossRef]
40. Van Gils, P. *Adaptive Incremental Backstepping Flight Control*; Delft University of Technology: Delft, The Netherlands, 2015.
41. Yun, Y.H.; Kim, C.-J.; Shin, K.C.; Yang, C.D.; Cho, I.J. Building the flight dynamic analysis program, HETLAS, for the development of helicopter FBW system. In Proceedings of the 1st Asian Australian Rotorcraft Forum and Exhibition, Busan, Korea, 12–15 February 2012.
42. Kim, C.-J.; Shin, K.C.; Yang, C.D.; Cho, I.J. Interface Features of Flight Dynamic Analysis Program, HETLAS, for the Development of Helicopter FBW System. In Proceedings of the 1st Asian Australian Rotorcraft Forum and Exhibition, Busan, Korea, 12–15 February 2012.
43. Naderi, K.; Rajamaki, J.; Hamalainen, P. RT-RRT$*$: A real-time path planning algorithm based on RRT$*$. In Proceedings of the 8th ACM SIGGRAPH Conference on Motion in Games, Paris, France, 16–18 November 2015; pp. 113–118.
44. Jordan, M.; Perez, A. *Optimal Bidirectional Rapidly-Exploring Random Trees*; MIT: Cambridge, MA, USA, 2013.